Spectroscopic Evidence for Periodic Magnetic Reconnection in a Solar Flare: Supplementary Information

William Ashfield IV[1], Vanessa Polito[2,3], Juraj Lörinčík[2,4], Bart De Pontieu[2,5,6], Georgios Chintzoglou[2], Souvik Bose[2,7,5,6], Nabil Freij[2,7], Luc Rouppe van der Voort[5,6], Reetika Joshi[8,9,6], and Jonas Thoen Faber[5,6]

[1]Southwest Research Institute, 1301 Walnut St, Suite 400, Boulder, CO 80302
[2]Lockheed Martin Solar and Astrophysics Laboratory, 3251 Hanover Street, Org. A021S, B. 203, Palo Alto, CA, 94304, USA
[3]Department of Physics, Oregon State University, 301 Weniger Hall, Corvallis, OR 97331
[4]Bay Area Environmental Research Institute
[5]Institute of Theoretical Astrophysics, University of Oslo, P.O. Box 1029 Blindern, N-0315 Oslo, Norway
[6]Rosseland Centre for Solar Physics, University of Oslo, P.O. Box 1029 Blindern, N-0315 Oslo, Norway
[7]SETI Institute, 339 Bernardo Avenue, Mountain View, CA 94043, USA
[8]NASA Goddard Space Flight Center, Heliophysics Science Division, Code 671, 8800 Greenbelt Road, Greenbelt, MD 20771, USA
[9]Department of Physics and Astronomy, George Mason University, Fairfax, VA 22030, USA

1 Fitting and evolution of Si IV line components

We found the complex profiles of the Si IV spectra well described by a six-Gaussian fit, with three negative components corresponding to the absorption lines superimposed on three positive components that account for the Si IV line and its blue and red wings. The multi-Gaussian fitting template, designed a priori with the `LMFIT`[1] Python package, was used to fit all Si IV spectra in the period under study. The fitting routine was fully automated, running through iterations of the fit with different components switched on and off by allowing the respective component intensities to be set to zero. The best fit was then determined by least-squares minimization. By inspecting the fits, we verified that the reduced χ^2 statistics converged to 1 in most spectra under study. The multi-Gaussian fitting routine was used to derive the evolution of the Si IV line for a single pixel-of-interest (POI) used in this study at [-635.93″, 262.81″], corresponding to the location where condensation downflows were the strongest. This location was identified via a preliminary analysis, where the Si IV velocity along the slit was calculated using a 1st-moment analysis of the spectral line over the wavelength range 1401.5–1404.0 Å. The velocity along the slit shown in Fig. 1 was also inferred using this method.

Multi-component Si IV profiles, albeit common among flare observations, do not typically show absorption lines. Previous investigations have found the presence of absorption features in so-called UV bursts, highly-localized transient brightenings seen in emerging active regions that have been attributed to reconnection in the photosphere[2,3] or chromosphere[4], and Alfvénic turbulence in the chromosphere[5]. Irrespective of its formation mechanism, these spectra have been shown to have absorption features matching those seen here: a self-absorption of Si IV and two narrow Fe II 1403.10 Å and 1403.13 Å absorption lines. Concerning the of Si IV self-abortion, this can either be attributed to optical-depth effects in chromospheric conditions[5] or the scattering of emission from plasma along the LOS[3]. The latter has also been used to describe the Fe II absorption lines, which would arise from cool gas lying atop the 80 kK plasma responsible for the Si IV emission[6]. Absorption of Fe II lines can also occur in chromospheric plasma with optical depths close to 0.1[5].

In the case of the present event, it is hard to quantify the conditions, namely a cool gas along the LOS or optical depth effects, that would result in these absorption features. For instance, cool, low-lying loops may exist along the LOS. A numerical study into chromospheric condensation was able to synthesize two-component Fe II 2814.45 Å profiles following an injection of electron beams[7], where each component arose from separate chromospheric depths due to the deposition height of high and low-energy electrons. As the condensation observed in this event also arises from electron deposition in the chromosphere, it is plausible that Si IV is formed at lower depths with cooler plasma along the LOS, thereby leading to the observed absorption features.

Regardless of the physical interpretation of these absorption features, the multi-Gaussian routine was primarily used to infer LOS plasma velocity in the low atmosphere. The central Gaussian was chosen for the analysis, as it is the most prominent emission component and shows clear oscillations over the observation window with minimal noise both pre- and post-flare. The evolution of the Gaussian fitting of the redshifted component, typically used to study Si IV condensation[8,9], also shows virtually the same oscillations in the POI, albeit noisier and at higher velocities (Supplementary Fig.1). Because the velocity oscillations of the central and redshifted Gaussian are in phase (c.f.; Figure 2, Supplementary Fig. 2), this suggests the plasma for the respective emission components is moving in tandem. Provided these components are formed in separate formation regions, this would further imply that different chromospheric regions are subjected to the repeated energy deposition driving the condensations, as evidenced by oscillations in Mg II and Ca II K . To the best of our knowledge, the peak redshift of the red-component (200.3 km s^{-1}) is the highest velocity of Si IV during a flare seen to date.

Oscillations of the individual Gaussian components (intensity, velocity, and FWHM) measured from the central Gaussian were also found to be correlated (Supplementary Fig. 2). In turn, this suggests the physical mechanisms underlying each component are also oscillating in phase. As has been discussed, the Doppler shift of the line is due to repeated energy injections in the form of non-thermal electrons, resulting in quasi-periodic downflows. Numerical simulations of condensation have shown these downflows to be in the form of radiative shocks propagating downward through the chromosphere[10,11]. This downward flowing shock naturally produces a corresponding region of enhanced plasma density, which could have implications for the broadening of the spectral line[12,13]. Variations in the FWHM of the line in flaring conditions could also be due to turbulence in the emitting region, as has been previously suggested[14]. QPPs of Si IV broadening measured in a separate event were found to contain periods of ≈10 s during the pre-flare phase, and were attributed to periodic variations in turbulence[15] (although no variations in the intensity or velocity were identified). Finally, we note that while propagating MHD waves could result in variations in the width of the line, we would expect to find the same $\pi/2$ phase relation between the intensity and velocity and a $P/2$ period in the FWHM (for a sausage mode wave), which is not seen here. Instead, our interpretation for the coherent oscillations in the Gaussian components is that it is caused by repeated, quasi-periodic, injections of energy into the chromosphere, which heat the plasma (increasing intensity), generate propagating downflows (changing velocity), and create compression and turbulence in the condensation region (enhancing FHWM). This interpretation also aligns with the generation of tearing modes in the corona, which has been linked to the onset of turbulence in the form of Si IV line broadening[16] (see Supplementary Section 3).

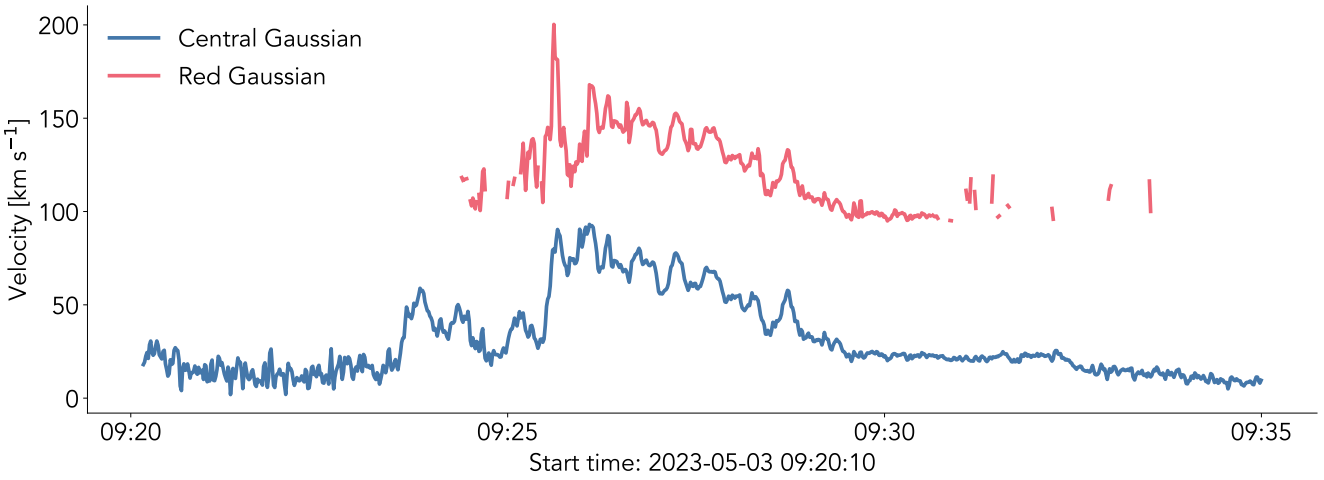

Supplementary Fig. 1. Evolution of the red and central components of the Si IV 1402.77 Å spectral line in the POI.

While the analysis of condensation taken from IRIS spectra is concentrated on a single pixel (POI), different IRIS pixels where the IRIS slit crossed the ribbon exhibited similar behavior. An example comparison is shown in Supplementary Fig. 3 that illustrates the velocity time series of the central Gaussian fit from two additional pixels, PX_u (green curve) and PX_l (yellow curve), corresponding to the upper and lower bounds of the IRIS ribbon pixels, respectively (see lower panel of Supplementary Fig. 4 for locations). To a large extent, the pulsations seen in the POI are present in the additional pixels. Differences between the velocities, while minor, can be attributed to several factors, including spatial inhomogeneities of the fine ribbon structure, the spatial evolution of the ribbon over time, and potential LOS effects of the local magnetic structure of the ribbon footpoints. Nevertheless, the consistent pulsation pattern across multiple IRIS pixels confirms that the observed condensation behavior represents a genuine physical phenomenon, not limited to our choice of the POI or instrumental effects. This result is further confirmed by the similarity of Ca II K velocity periods across the entire ribbon structure.

2 Bi-modal periodicities in QPP map

Analysis of oscillations in Ca II K condensation revealed that while most ribbon pixels displayed a single dominant period, 20% showed bimodal QPP behavior with two significant peaks in their period power spectrum. Supplementary Fig. 5(a) maps these secondary QPP periods and their spatial distribution. While this distribution is not as well-defined as the one seen with the primary periods, they peak at ≈25 and ≈42 s. Calculating the period ratios at each bimodal QPP pixel location yields the map and distribution shown in Fig. 5(b). Here, we find two distinct peaks at 0.67 and 1.57, respectively. Like the primary periods, neither the secondary periods nor their ratios demonstrate any spatial organization along the ribbon.

The ratios of 0.67 and 1.57 are notable as they correspond to near integer ratios of 2:3 and 3:2, respectively. It is tempting to speculate about the processes that drive bi-modal QPPs with such period ratios. They could suggest a coupling of modes between the primary and secondary QPP periods along the ribbon. In contrast to a simple harmonic system, which would have integer ratios of 1:n[17], the 2:3 and 3:2 ratios can be characteristic of systems with nonlinear wave interactions[18–21]. In our speculative interpretation, the primary 34.1 s oscillation would be directly driven by the electron acceleration mechanism, as supported by the correlation with HXR signals, while the emergence of secondary periods in rational ratios could be caused by a nonlinear response of the chromospheric plasma to impulsive heating. The presence of these rational ratios, occurring in a substantial fraction of ribbon pixels that are evenly distributed throughout the ribbon, would then indicate that such couplings may be a component of the overall energy transport and dissipation mechanism during the impulsive phase of solar flares, possibly linked to the fundamental ways MHD modes can naturally arise from quasi-periodic impulsive forcing.

3 Connection between observations and the tearing mode instability

The tearing mode instability arises when a current sheet approaches a critical aspect ratio, causing the sheet to decompose into a series of magnetic islands, or plasmoids[22,23]. The formation of plasmoids creates multiple X-points between adjacent islands along the current sheet, facilitating fast reconnection. Plasmoids can also cascade into smaller scales[24] or coalesce into larger islands[25], creating an environment where reconnection becomes fundamentally bursty in the process[26]. This mechanism offers a viable framework for oscillatory reconnection in addition to efficient particle acceleration in flares[27], and has been used to

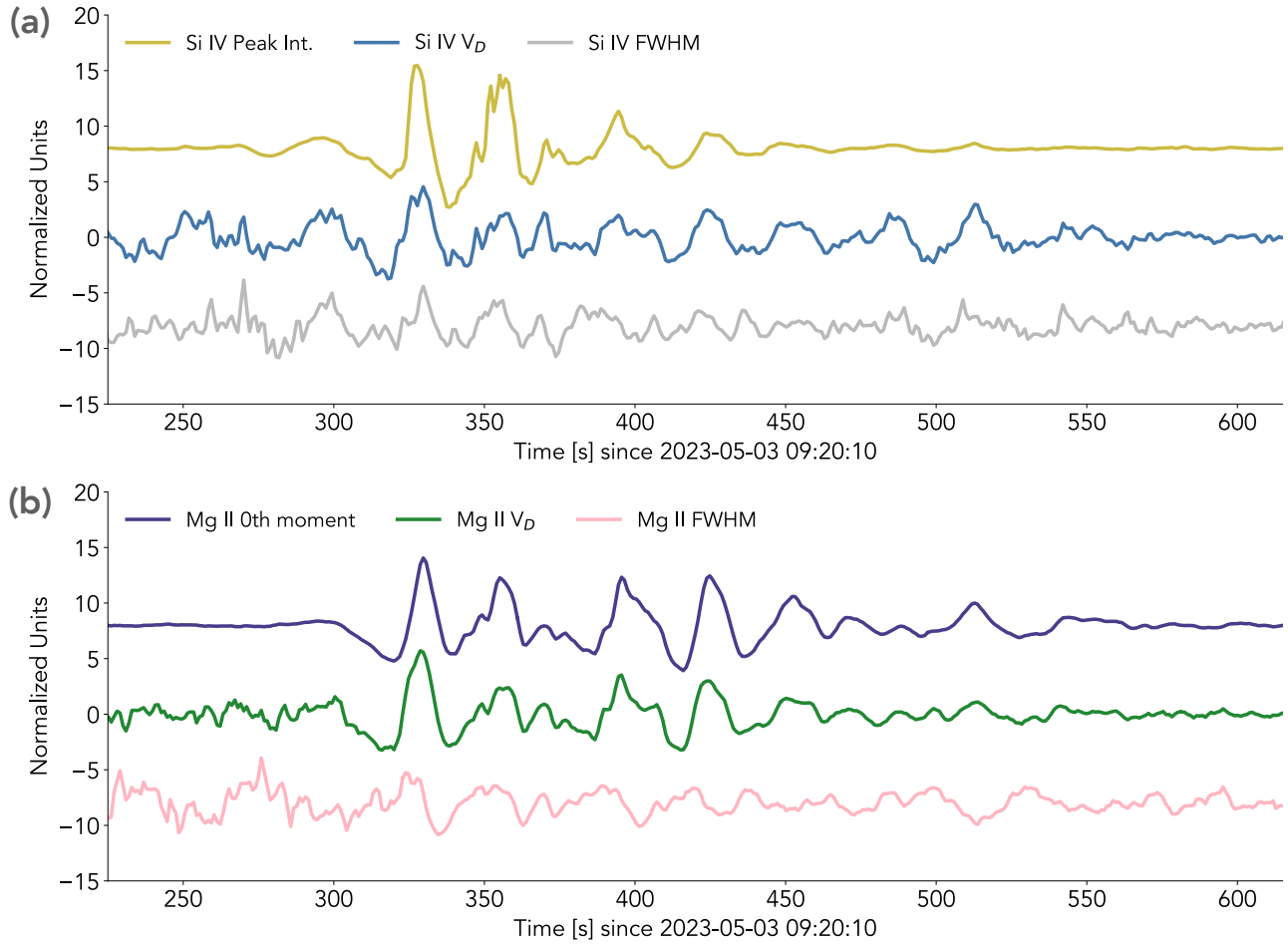

Supplementary Fig. 2. Evolution of detrended line components from the central Si IV 1402.77 Å Gaussian (a) and Mg II 2791.60 Å moments (b) in the POI.

explain QPPs in HXR and radio in flares[28,29].

While EUV images of current sheets during flares constitute direct observational evidence of plasmoids[29–31], indirect evidence is also possible through measuring the structure and dynamics of flare ribbons[16,32]. As ribbons are widely considered to be the aggregate of individual flare loop footpoints, instabilities present in the corona would likely be reflected in the chromosphere following the transport of energy generated via a fragmented reconnection process. One such indirect observation is the presence of fine ribbon structure. Recent work[33] using observations taken with SST/CHROMIS found small-scale periodic blobs of plasma along the flare ribbon, which were attributed to current sheet tearing. This interpretation was based on the results of a numerical study[34] that was able to reproduce such features as a response to tearing modes using an analytical 3D flare model.

Here, we find similar observations in the high-resolution Ca II K data, where the structure of the flare ribbon footpoints consists of finger-like striations along the ribbon's elongation axis. Supplementary Fig. 6 shows an example of this behavior at one time, where there appears to be a quasi-periodic spatial pattern similar to the kernels analyzed by[33]. The loop footpoints also demonstrate dynamic behavior typical of the "breaking wavelike" perturbations of the flare ribbon plasma (see Supplementary Video 1), which was also predicted by an analytical model[34].

A previous investigation[32] using IRIS data found tearing modes could also explain the "sawtooth pattern" observed when small-scale ribbon structure cross the slit, which was later affirmed by a follow-up numerical study[35]. Condensation oscillations were also found in the IRIS Si IV line, where both the sawtooth oscillations and condensation velocities were quasi-periodic with periodicities of ≈140 s. In the current work, the evolution of Si IV intensity and velocity along the spectrograph slit (Supplementary Fig. 4) is reminiscent of the same 'sawtooth pattern', best seen before 09:25 UT.

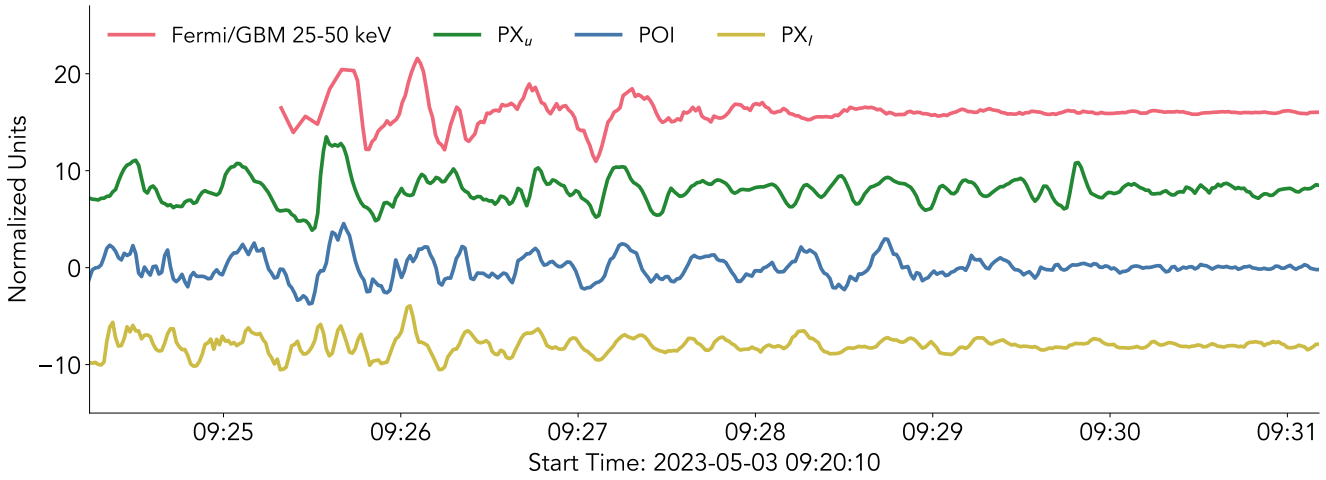

Supplementary Fig. 3. Detrended Si IV 1402.77 Å velocities taken from the POI (blue) and two additional pixels: PX$_u$ (green) and PX$_l$ (yellow). Detrended 25-50 keV HXRs (red) are shown for context. The locations of each pixel are shown in Supplementary Fig. 4.

A comparison between the morphological and temporal characteristics of these features and those seen in past studies supports the interpretation that they are lower atmospheric manifestations of plasmoid-mediated reconnection occurring in coronal current sheets. The primary ≈35 s oscillations we observe in ribbon velocities likely correspond to this reconnection process, potentially reflecting the characteristic growth time of the tearing modes or the coalescence of magnetic islands[25].

4 Wavelet Analysis

The routine outlined in Methods for determining QPP periodicity was applied to the oscillatory signals referenced in Results. The outputs of this routine depicting the original signal, detrended signal, slowly varying component, and the results from the wavelet analysis and Lomb-Scargle periodogram are shown below for the following timeseries: CHROMIS Ca II K POI mean V_D (Supplementary Fig. 7), IRIS Mg II 2791.6 Å V_D (Supplementary Fig. 8), Fermi/GBM 25-50 keV (Supplementary Fig. 9), and IRIS Fe XXI 1354.08 Å peak intensity (Supplementary Fig. 10), velocity (Supplementary Fig. 11), and FWHM (Supplementary Fig. 12).

References

1. Newville, M. *et al.* Lmfit: Non-linear least-squares minimization and curve-fitting for python, DOI: 10.5281/zenodo.15014437 (2025).
2. Peter, H. *et al.* Hot explosions in the cool atmosphere of the Sun. *Science* **346**, 1255726, DOI: 10.1126/science.1255726 (2014). 1410.5842.
3. Vissers, G. J. M., Rouppe van der Voort, L. H. M., Rutten, R. J., Carlsson, M. & De Pontieu, B. Ellerman Bombs at High Resolution. III. Simultaneous Observations with IRIS and SST. *ApJ* **812**, 11, DOI: 10.1088/0004-637X/812/1/11 (2015). 1507.00435.
4. Hansteen, V. *et al.* Ellerman bombs and UV bursts: transient events in chromospheric current sheets. *AAP* **626**, A33, DOI: 10.1051/0004-6361/201935376 (2019). 1904.11524.
5. Judge, P. G. UV Spectra, Bombs, and the Solar Atmosphere. *ApJ* **808**, 116, DOI: 10.1088/0004-637X/808/2/116 (2015). 1506.08336.
6. Pereira, T. M. D., Carlsson, M., De Pontieu, B. & Hansteen, V. The Formation of IRIS Diagnostics. IV. The Mg II Triplet Lines as a New Diagnostic for Lower Chromospheric Heating. *ApJ* **806**, 14, DOI: 10.1088/0004-637X/806/1/14 (2015). 1504.01733.
7. Graham, D. R. *et al.* Spectral Signatures of Chromospheric Condensation in a Major Solar Flare. *ApJ* **895**, 6, DOI: 10.3847/1538-4357/ab88ad (2020). 2004.05075.

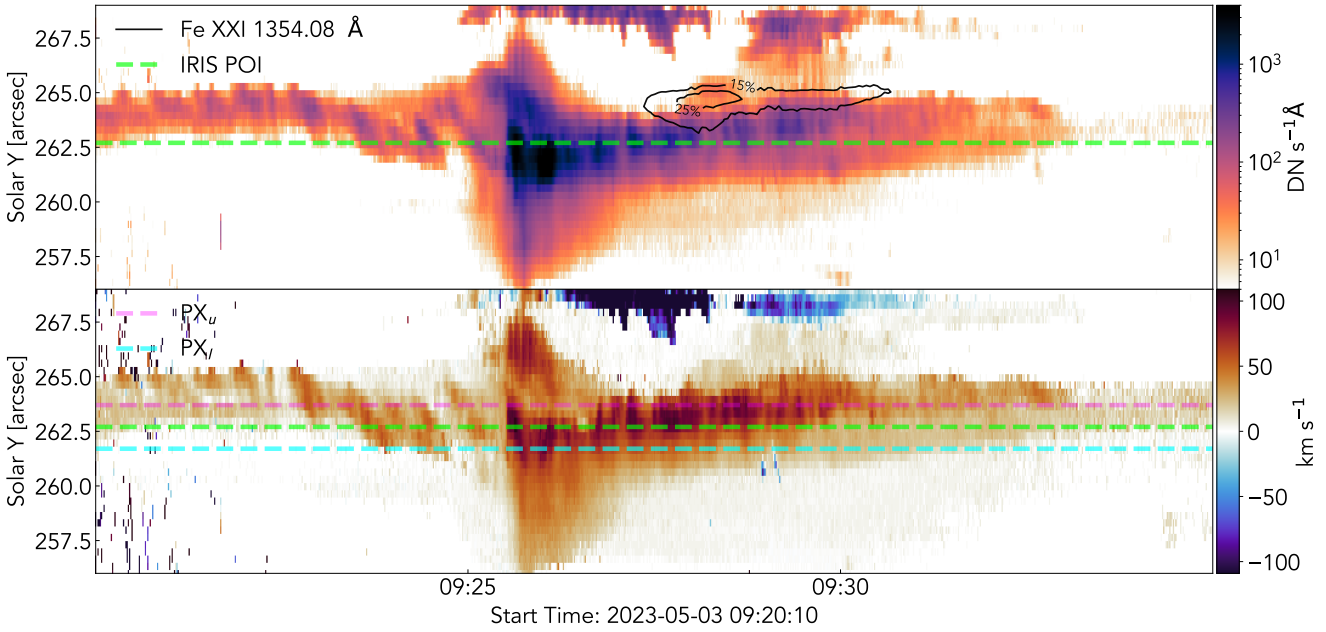

Supplementary Fig. 4. Temporal evolution of Si IV 1402.77 Å along the IRIS spectrograph slit. Each panel is a time-distance stack plot over the portion of the slit covering the flare ribbon. The top panel shows integrated intensity (0th-moment), with the green dashed line indicating the POI. Black contours show the region of Fe XXI 1354.08 Å emission at 15% and 25% peak intensity, respectively. The bottom panel shows the 1st moment velocity. Pink and cyan dashed lines show the PX_u and PX_l locations.

8. Ashfield, W. H., IV, Longcope, D. W., Zhu, C. & Qiu, J. Connecting Chromospheric Condensation Signatures to Reconnection-driven Heating Rates in an Observed Flare. *ApJ* **926**, 164, DOI: 10.3847/1538-4357/ac402d (2022). 2112.02150.

9. Lörinčík, J., Polito, V., De Pontieu, B., Yu, S. & Freij, N. Rapid variations of Si IV spectra in a flare observed by interface region imaging spectrograph at a sub-second cadence. *Front. Astron. Space Sci.* **9**, 334, DOI: 10.3389/fspas.2022.1040945 (2022). 2210.12205.

10. Fisher, G. H. Chromospheric downflow velocities as a diagnostic in solar flares. *Sol. Phys.* **113**, 307–311, DOI: 10.1007/BF00147715 (1987).

11. Ashfield, W. H. & Longcope, D. W. Relating the Properties of Chromospheric Condensation to Flare Energy Transported by Thermal Conduction. *ApJ* **912**, 25, DOI: 10.3847/1538-4357/abedb4 (2021).

12. Kowalski, A. F., Allred, J. C., Daw, A., Cauzzi, G. & Carlsson, M. The Atmospheric Response to High Nonthermal Electron Beam Fluxes in Solar Flares. I. Modeling the Brightest NUV Footpoints in the X1 Solar Flare of 2014 March 29. *ApJ* **836**, 12, DOI: 10.3847/1538-4357/836/1/12 (2017). 1609.07390.

13. Kowalski, A. F. *et al.* The Atmospheric Response to High Nonthermal Electron-beam Fluxes in Solar Flares. II. Hydrogen-broadening Predictions for Solar Flare Observations with the Daniel K. Inouye Solar Telescope. *ApJ* **928**, 190, DOI: 10.3847/1538-4357/ac5174 (2022). 2201.13349.

14. Polito, V., Testa, P. & De Pontieu, B. Can the Superposition of Evaporative Flows Explain Broad Fe XXI Profiles during Solar Flares? *ApJL* **879**, L17, DOI: 10.3847/2041-8213/ab290b (2019).

15. Jeffrey, N. L. S., Fletcher, L., Labrosse, N. & Simões, P. J. A. The development of lower-atmosphere turbulence early in a solar flare. *Sci. Adv.* **4**, 2794, DOI: 10.1126/sciadv.aav2794 (2018). 1812.09906.

16. French, R. J., Matthews, S. A., Jonathan Rae, I. & Smith, A. W. Probing Current Sheet Instabilities from Flare Ribbon Dynamics. *ApJ* **922**, 117, DOI: 10.3847/1538-4357/ac256f (2021). 2109.03753.

17. Nakariakov, V. M. & Kolotkov, D. Y. Magnetohydrodynamic Waves in the Solar Corona. *Annu. Rev. Astron. Astrophys.* **58**, 441–481, DOI: 10.1146/annurev-astro-032320-042940 (2020).

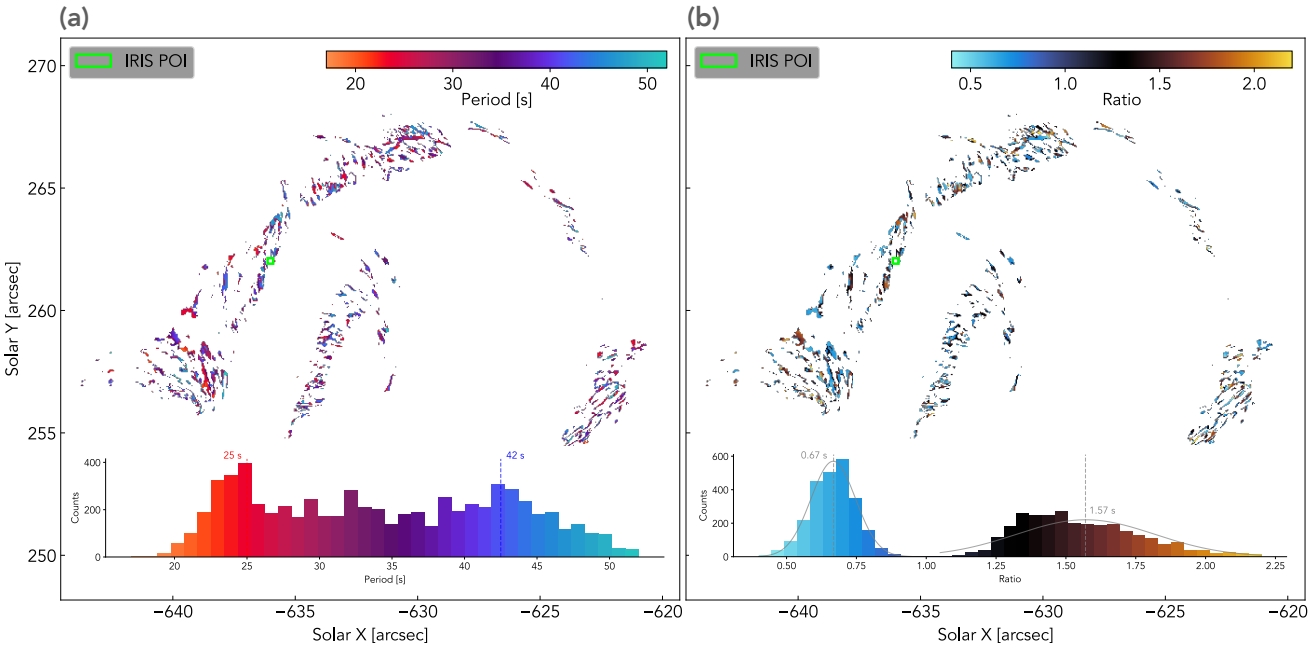

Supplementary Fig. 5. Map of secondary Ca II K periods and corresponding ratios. The left panel shows the map of secondary periods from pixels containing a bi-modal global wavelet power spectrum. The inset histogram shows the spread of periods, with the dashed lines indicating the approximate peaks in the distribution. The right panel is the map of the secondary-to-primary period ratios. The inset histogram shows the spread of ratios, with normal distribution fits to the distinct ratio spreads (gray curve). Gray-dashed lines indicate the peaks of the normal distribution fits.

18. Kato, S. Wave-Warp Resonant Interactions in Relativistic Disks and kHz QPOs. *Publ. Astron. Soc. Jpn.* **56**, 559–567, DOI: 10.1093/pasj/56.3.599 (2004).

19. Rebusco, P. Twin Peaks kHz QPOs: Mathematics of the 3:2 Orbital Resonance. *Publ. Astron. Soc. Jpn.* **56**, 553–557, DOI: 10.1093/pasj/56.3.553 (2004). astro-ph/0403341.

20. Horák, J. The autoparametric 3:2 resonance in conservative systems. *Astron. Nachrichten* **326**, 824–829, DOI: 10.1002/asna.200510421 (2005). astro-ph/0510605.

21. Kluzniak, W., Abramowicz, M. A., Bursa, M. & Török, G. QPOs and Resonance in Accretion Disks. In *Revista Mexicana de Astronomia y Astrofisica, vol. 27*, vol. 27 of *Revista Mexicana de Astronomia y Astrofisica Conference Series*, 18–25 (2007).

22. Furth, H. P., Killeen, J. & Rosenbluth, M. N. Finite-Resistivity Instabilities of a Sheet Pinch. *Phys. Fluids* **6**, 459–484, DOI: 10.1063/1.1706761 (1963).

23. Biskamp, D. Magnetic reconnection via current sheets. *Phys. Fluids* **29**, 1520–1531, DOI: 10.1063/1.865670 (1986).

24. Bárta, M., Büchner, J., Karlický, M. & Kotrč, P. Spontaneous Current-layer Fragmentation and Cascading Reconnection in Solar Flares. II. Relation to Observations. *ApJ* **730**, 47, DOI: 10.1088/0004-637X/730/1/47 (2011). 1011.6069.

25. Jelínek, P., Karlický, M., Van Doorsselaere, T. & Bárta, M. Oscillations Excited by Plasmoids Formed During Magnetic Reconnection in a Vertical Gravitationally Stratified Current Sheet. *ApJ* **847**, 98, DOI: 10.3847/1538-4357/aa88a6 (2017). 1703.06674.

26. Priest, E. R. REVIEW ARTICLE: The magnetohydrodynamics of current sheets. *Reports on Prog. Phys.* **48**, 955–1090, DOI: 10.1088/0034-4885/48/7/002 (1985).

27. Drake, J. F., Swisdak, M., Che, H. & Shay, M. A. Electron acceleration from contracting magnetic islands during reconnection. *Nature* **443**, 553–556, DOI: 10.1038/nature05116 (2006).

28. Corchado Albelo, M. F., Kazachenko, M. D. & Lynch, B. J. Inferring Fundamental Properties of the Flare Current Sheet Using Flare Ribbons: Oscillations in the Reconnection Flux Rates. *ApJ* **965**, 16, DOI: 10.3847/1538-4357/ad25f4 (2024). 2402.03567.

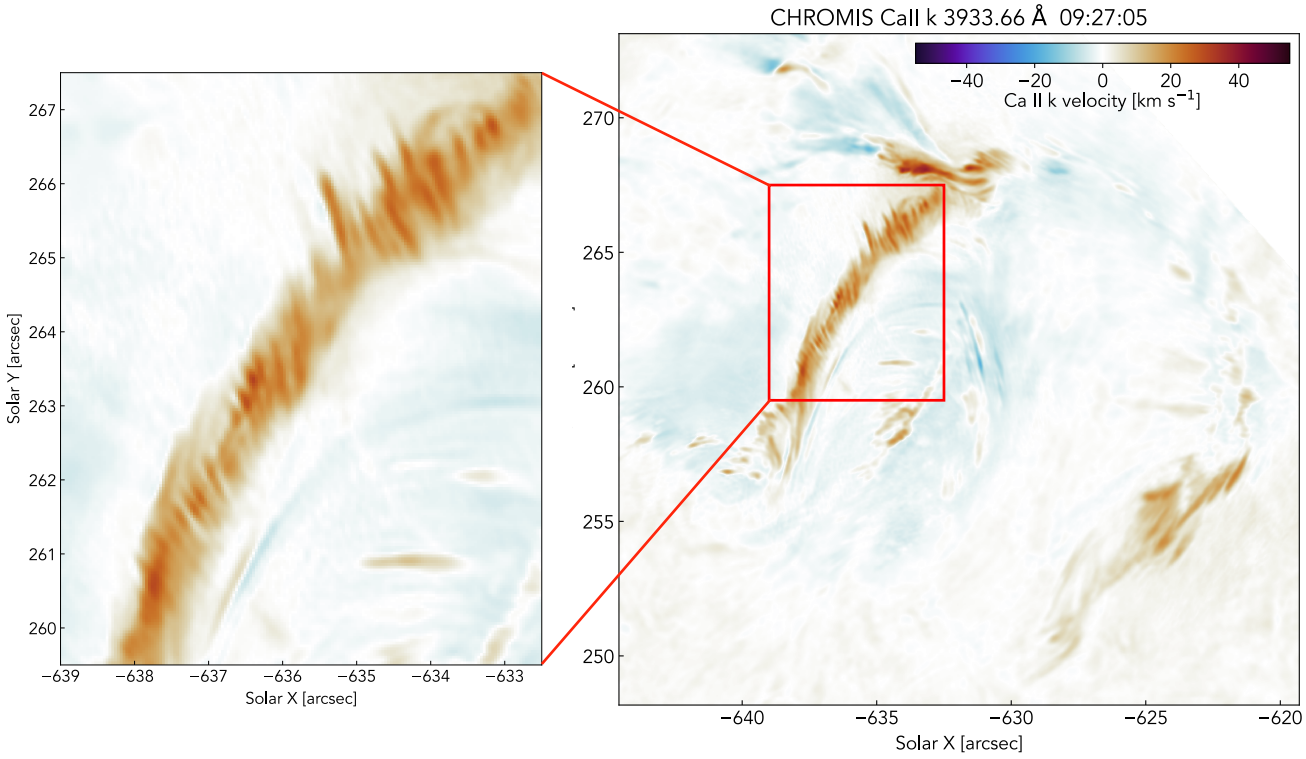

Supplementary Fig. 6. Example of fine-scale ribbon structure. The left panel shows the Ca II K velocity over the ROI at a time during the impulsive phase of the flare. A section of the ribbon depicting finger-like striations constituting the ribbon structure is enlarged on the right.

29. Kumar, P., Karpen, J. T. & Dahlin, J. T. X-Ray/Radio Quasiperiodic Pulsations Associated with Plasmoids in Solar Flare Current Sheets. *ApJ* **980**, 158, DOI: 10.3847/1538-4357/ada293 (2025). 2412.05193.

30. Tripathi, D., Reeves, K. K., Gibson, S. E., Srivastava, A. & Joshi, N. C. SDO/AIA Observations of a Partially Erupting Prominence. *ApJ* **778**, 142, DOI: 10.1088/0004-637X/778/2/142 (2013). 1310.0162.

31. Kumar, P., Karpen, J. T., Antiochos, S. K., Wyper, P. F. & DeVore, C. R. First Detection of Plasmoids from Breakout Reconnection on the Sun. *ApJL* **885**, L15, DOI: 10.3847/2041-8213/ab45f9 (2019). 1909.06637.

32. Brannon, S. R., Longcope, D. W. & Qiu, J. Spectroscopic Observations of an Evolving Flare Ribbon Substructure Suggesting Origin in Current Sheet Waves. *ApJ* **810**, 4, DOI: 10.1088/0004-637X/810/1/4 (2015). 1507.01554.

33. Thoen Faber, J. *et al.* High-resolution observational analysis of flare ribbon fine structures. *AAP* **693**, A8, DOI: 10.1051/0004-6361/202452370 (2025). 2411.18233.

34. Wyper, P. F. & Pontin, D. I. Is Flare Ribbon Fine Structure Related to Tearing in the Flare Current Sheet? *ApJ* **920**, 102, DOI: 10.3847/1538-4357/ac1943 (2021). 2108.10966.

35. Parker, J. & Longcope, D. Modeling a Propagating Sawtooth Flare Ribbon Structure as a Tearing Mode in the Presence of Velocity Shear. *ApJ* **847**, 30, DOI: 10.3847/1538-4357/aa8908 (2017). 1709.04534.

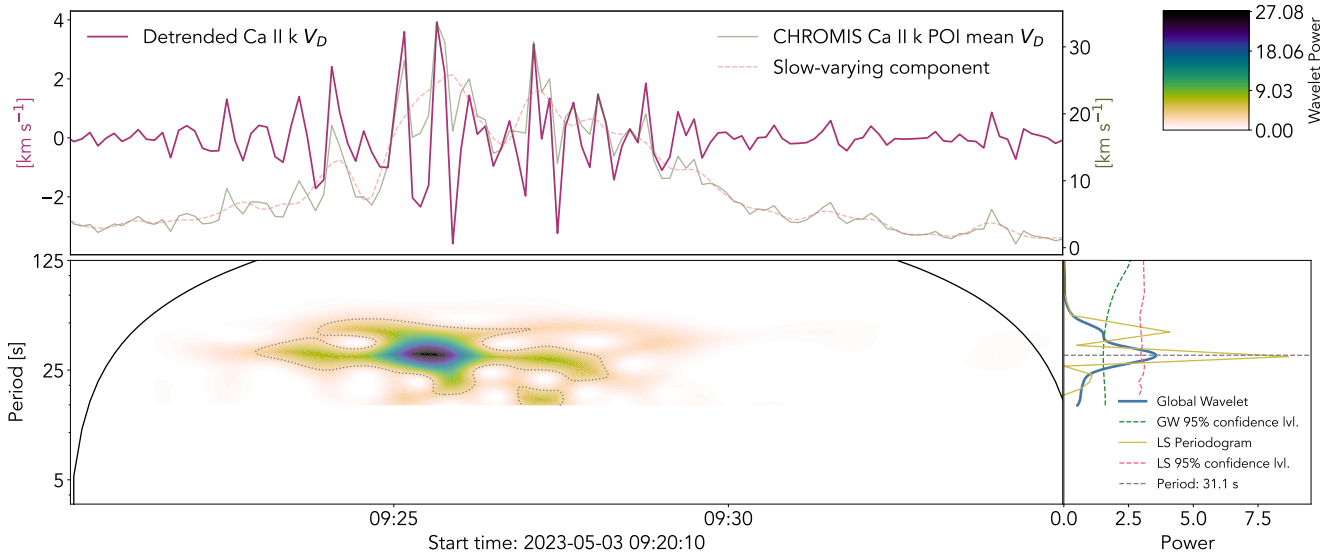

Supplementary Fig. 7. QPP analysis results for the averaged POI Ca II K velocity.

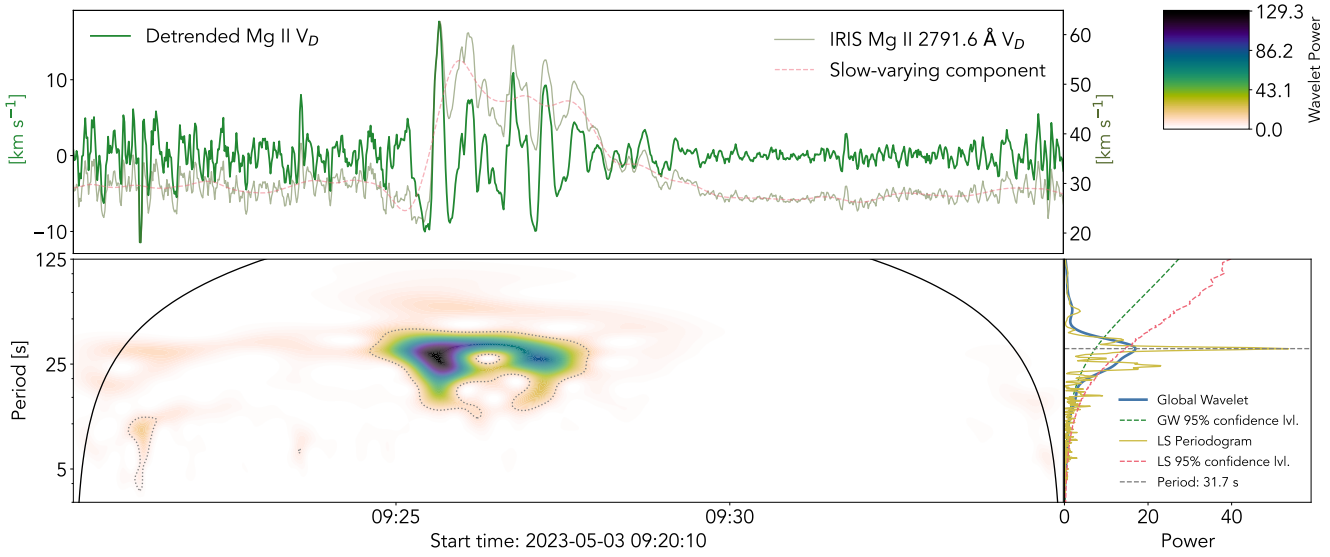

Supplementary Fig. 8. QPP analysis results for the Mg II 2791.6 Å velocity.

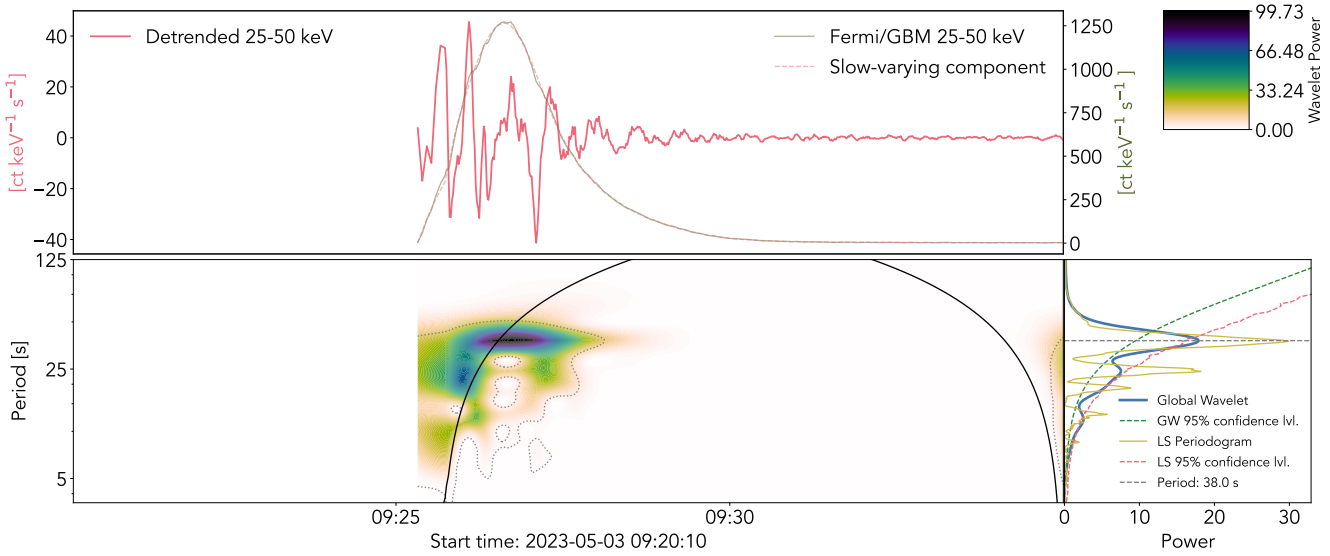

Supplementary Fig. 9. QPP analysis results for the 25-50 keV HXR fluctuations.

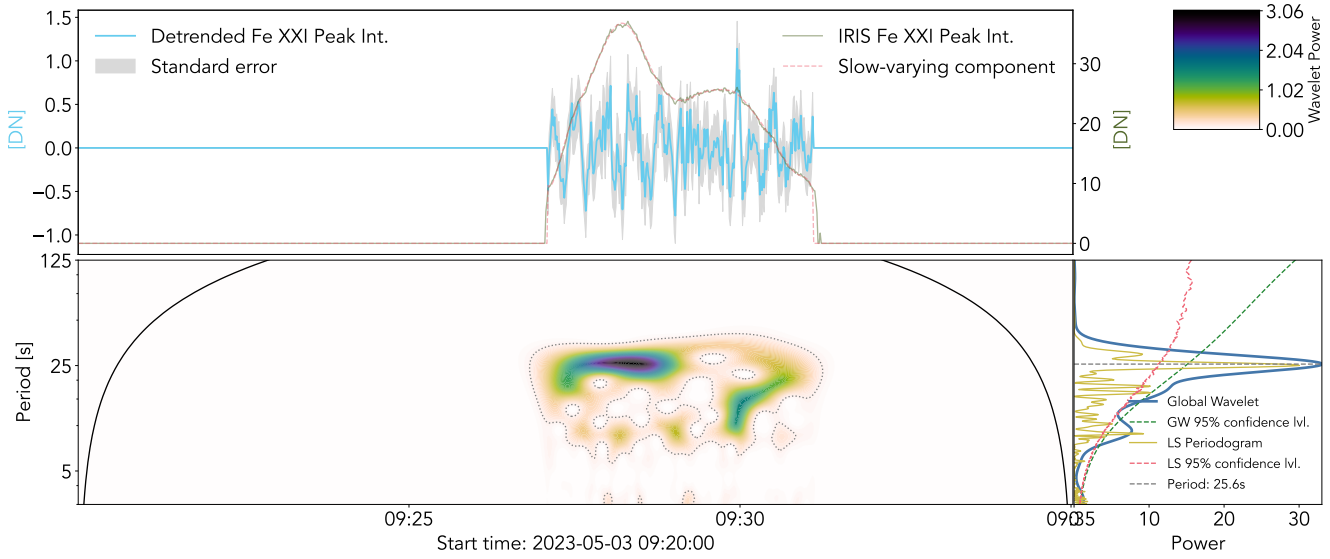

Supplementary Fig. 10. QPP analysis results for the Fe XXI 1354.08 Å peak intensity.

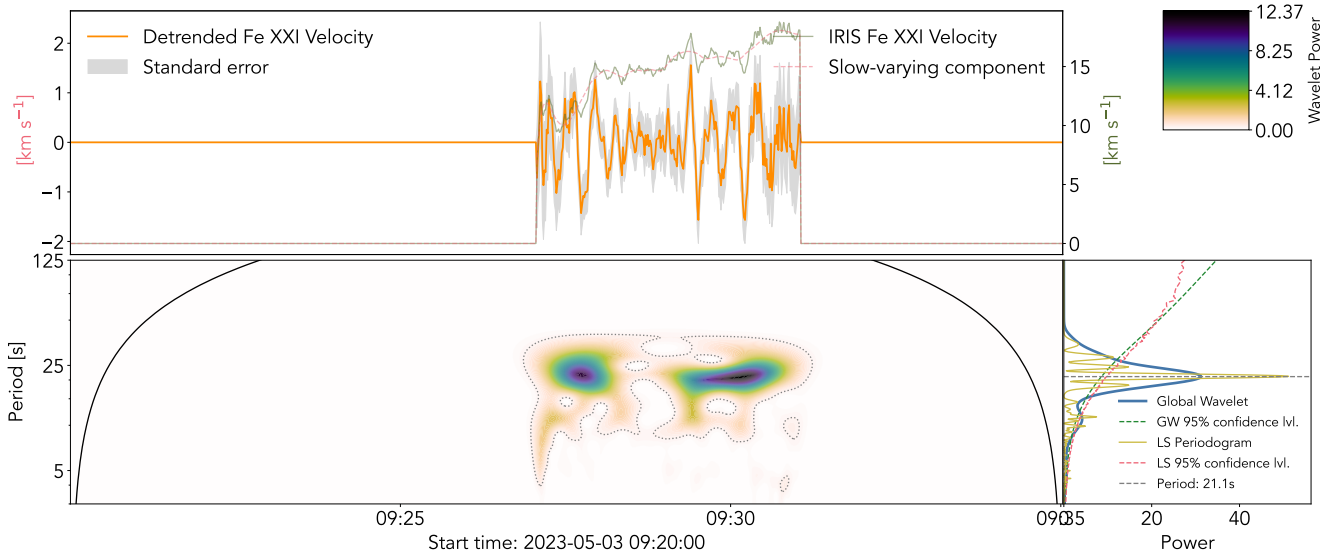

Supplementary Fig. 11. QPP analysis results for the Fe XXI 1354.08 Å velocity.

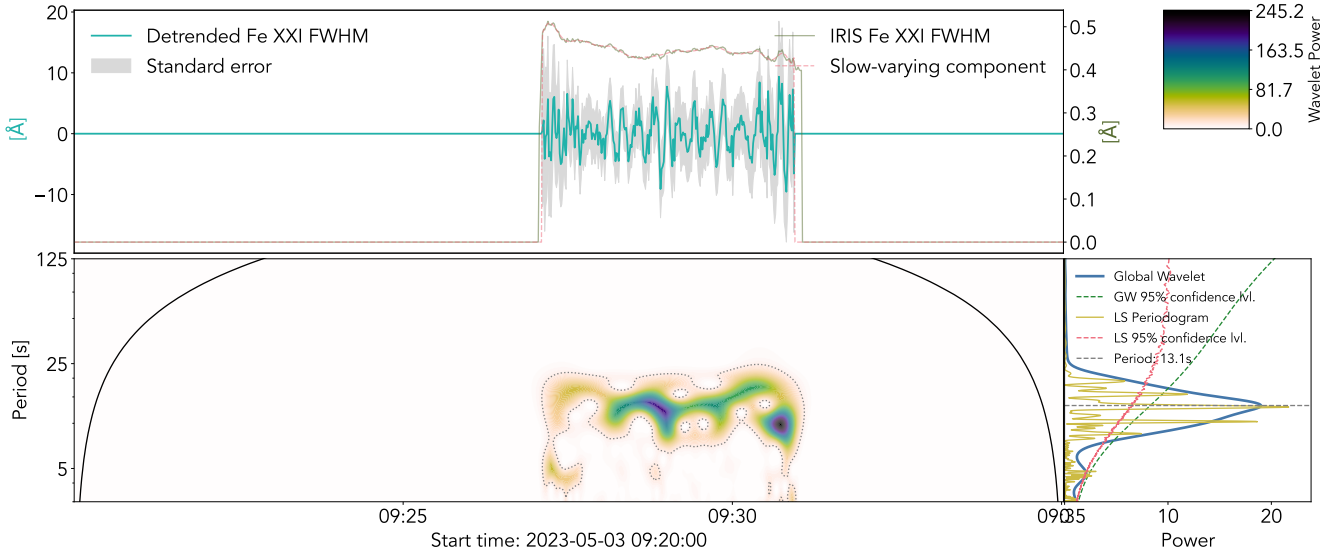

Supplementary Fig. 12. QPP analysis results for the Fe XXI 1354.08 Å FWHM.